

Realization of Large Electric Polarization and Strong Magnetolectric Coupling in $\text{BiMn}_3\text{Cr}_4\text{O}_{12}$

Long Zhou, Jianhong Dai, Yisheng Chai, Huimin Zhang, Shuai Dong, Huibo Cao, Stuart Calder, Yunyu Yin, Xiao Wang, Xudong Shen, Zhehong Liu, Takashi Saito, Yuichi Shimakawa, Hajime Hojo, Yuichi Ikuhara, Masaki Azuma, Zhiwei Hu, Young Sun, Changqing Jin, and Youwen Long*

Magnetolectric multiferroics have received much attention in the past decade due to their interesting physics and promising multifunctional performance. For practical applications, simultaneous large ferroelectric polarization and strong magnetolectric coupling are preferred. However, these two properties have not been found to be compatible in the single-phase multiferroic materials discovered as yet. Here, it is shown that superior multiferroic properties exist in the A-site ordered perovskite $\text{BiMn}_3\text{Cr}_4\text{O}_{12}$ synthesized under high-pressure and high-temperature conditions. The compound experiences a ferroelectric phase transition ascribed to the $6s^2$ lone-pair effects of Bi^{3+} at around 135 K, and a long-range antiferromagnetic order related to the Cr^{3+} spins around 125 K, leading to the presence of a type-I multiferroic phase with huge electric polarization. On further cooling to 48 K, a type-II multiferroic phase induced by the special spin structure composed of both Mn- and Cr-sublattices emerges, accompanied by considerable magnetolectric coupling. $\text{BiMn}_3\text{Cr}_4\text{O}_{12}$ thus provides a rare example of joint multiferroicity, where two different types of multiferroic phases develop subsequently so that both large polarization and significant magnetolectric effect are achieved in a single-phase multiferroic material.

Magnetolectric multiferroics have received much attention in the past decade due to the interesting physics and promising multifunctional performances such as spintronic devices, nonvolatile memory devices, solid-state transformers as well as strong magnetolectric (ME) effects where the electric polarization (P) can be tuned by magnetic field (H) or magnetization (M) can be tuned by electric field (E) etc.^[1–8] Based on the different origins of ferroelectricity, single-phase multiferroic (MF) materials can be classified into two categories:^[9] type-I and type-II. In the type-I MF, the ferroelectricity and magnetism originate from different sources. As a result, the ME coupling coefficient $\alpha = dP/dH$ is relatively small, although the values of electric polarization and magnetization probably are both large enough. A well-known example of type-I MF is BiFeO_3 ,^[10] in which the lone-pair

Dr. L. Zhou, Dr. J. H. Dai, Prof. Y. S. Chai, Dr. Y. Y. Yin, Dr. X. Wang, Dr. X. D. Sheng, Dr. Z. H. Liu, Prof. Y. Sun, Prof. C. Q. Jin, Prof. Y. W. Long
Beijing National Laboratory for Condensed Matter Physics
Institute of Physics
Chinese Academy of Sciences
Beijing 100190, China
E-mail: ywlong@iphy.ac.cn

Dr. L. Zhou, Dr. J. H. Dai, Prof. Y. S. Chai, Dr. Y. Y. Yin, Dr. X. Wang, Dr. X. D. Sheng, Dr. Z. H. Liu, Prof. Y. Sun, Prof. C. Q. Jin, Prof. Y. W. Long
School of Physical Sciences
University of Chinese Academy of Sciences
Beijing 100190, China

Dr. H. M. Zhang, Prof. S. Dong
School of Physics
Southeast University
Nanjing 211189, China

Dr. H. B. Cao, Dr. S. Calder
Quantum Condensed Matter Division
Oak Ridge National Laboratory
Oak Ridge, TN 37831, USA


Prof. T. Saito, Prof. Y. Shimakawa
Institute for Chemical Research
Kyoto University
Uji, Kyoto 611-0011, Japan

Prof. H. Hojo, Prof. M. Azuma
Materials and Structures Laboratory
Tokyo Institute of Technology
4259 Nagatsuta, Midori-ku, Yokohama 226-8503, Japan

Prof. Y. Ikuhara
Institute of Engineering Innovation
University of Tokyo
Bunkyo, Tokyo 113-8656, Japan

Dr. Z. Hu
Max Planck Institute for Chemical Physics of Solids
Dresden 01187, Germany

Prof. C. Q. Jin, Prof. Y. W. Long
Collaborative Innovation Center of Quantum Matter
Beijing 100190, China

 The ORCID identification number(s) for the author(s) of this article can be found under <https://doi.org/10.1002/adma.201703435>.

DOI: 10.1002/adma.201703435

active Bi^{3+} ions and the magnetic Fe^{3+} ions lead to ferroelectricity and long-range spin ordering at different temperatures, respectively. However, its α value is only estimated to be 2–5 ps m^{-1} even under very high magnetic field.^[11] In contrast, for the type-II MF, the ferroelectric (FE) polarization is induced by special spin textures such as the zigzag-type antiferromagnetic (AFM) ordering,^[12] cycloidal, or transverse conical spin structure.^[13–15] Consequently, the magnetism and ferroelectricity can strongly couple with each other. However, compared with the type-I MF, the electric polarization of the type-II MF is often reduced by several orders of magnitude. For potential applications of MF materials, both the large ferroelectric polarization and strong magnetoelectric coupling are highly desired. However, these two merits are usually found to be incompatible in the single-phase MF materials discovered so far because the two different types of MF phases mentioned above hardly coexist in a single-phase material. This incompatibility is a big obstacle that challenges the practical applications.

Recently, the ME multiferroicity was observed in an A-site ordered perovskite oxide $\text{LaMn}_3\text{Cr}_4\text{O}_{12}$ (LMCO), where two AFM transitions arising from the A-site Mn^{3+} and the B-site Cr^{3+} spins take place at 150 and 50 K, respectively.^[16] Although the cubic symmetry of LMCO with inversion center is unexpected to exhibit ferroelectricity, the peculiar AFM spin alignment pattern along [111] direction can break the space inversion symmetry and cause a type-II MF phase below 50 K.^[16,17] As expected, LMCO shows a remarkable ME effect ($\alpha \approx 10 \text{ ps m}^{-1}$), but the electric polarization value itself is very small ($1.5 \times 10^{-3} \mu\text{C cm}^{-2}$ at zero field).^[16] Since the stereochemical effects of $6s^2$ lone-pair electrons such as Bi^{3+} and Pb^{2+} could induce large FE polarization as observed in the type-I MF BiFeO_3 ($10\text{--}100 \mu\text{C cm}^{-2}$)^[9,18] and $\text{PbFe}_{0.5}\text{Nb}_{0.5}\text{O}_3$ ($\approx 25 \mu\text{C cm}^{-2}$),^[19] a new compound $\text{BiMn}_3\text{Cr}_4\text{O}_{12}$ (BMCO) was thus intentionally designed and prepared. Interestingly, a FE phase transition caused by the lone-pair active Bi^{3+} is found to occur in BMCO around 135 K. On further cooling to 125 K, the B-site Cr^{3+} spins order antiferromagnetically, giving rise to the presence of a type-I MF phase with large electric polarization. Subsequently, the A-site Mn^{3+} ions trigger another AFM ordering at 48 K. More interesting, the AFM structure composed of both Mn^{3+} and Cr^{3+} ions in BMCO is similar with that of LMCO, as shown in Figure S1 (Supporting Information). As a result, the spin structure of BMCO breaks the space inversion symmetry and induces a type-II MF phase below 48 K. Since type-I and type-II MF phases coexist, both large FE polarization and strong ME coupling are realized in the current BMCO.

Compared with a simple ABO_3 perovskite, the A-site ordered perovskite has a chemical formula $\text{AA}'_3\text{B}_4\text{O}_{12}$, where three quarters of the originally 12 coordinated A site are occupied by a transition-metal ion A' with square coordinated $\text{A}'\text{O}_4$ unit (see Figure 1a). The BO_6 octahedra are highly tilted to match the smaller ionic size of the A' -site transition metal. High pressure is thus often necessary to stabilize this heavily distorted perovskite structure. The polycrystalline BMCO was prepared at 8 GPa and 1373 K, as described in the Experimental and Theoretical Section. High-resolution synchrotron X-ray diffraction (SXR), neutron powder diffraction (NPD), and selected area electron diffraction (SAED) were used to characterize the crystal structure. Figure 1b shows the SXR pattern measured

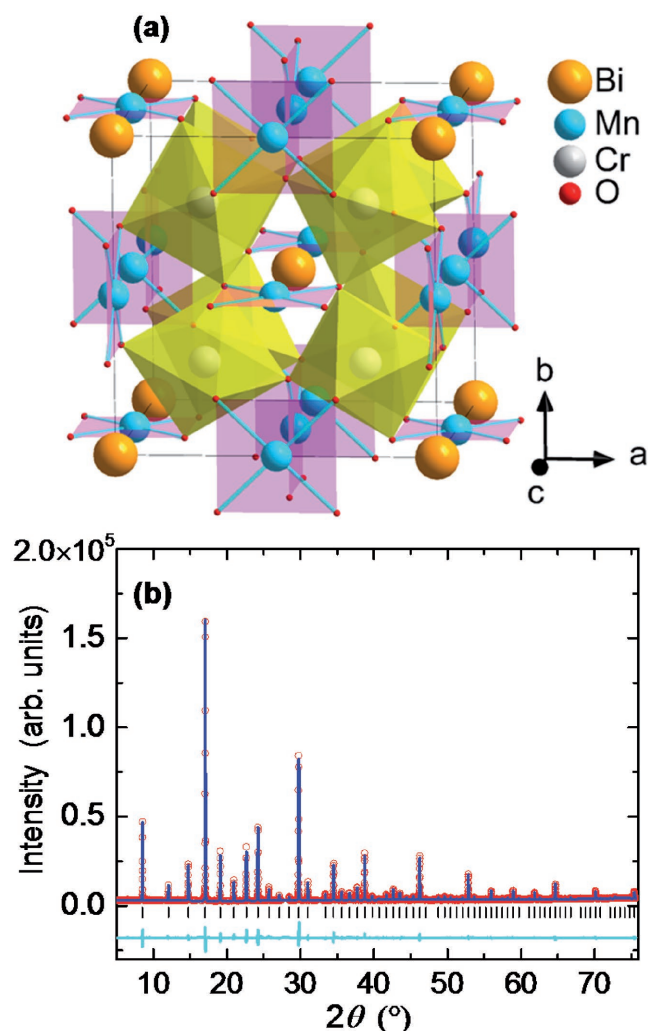


Figure 1. a) Schematic illustration for the crystal structure of A-site ordered perovskite BMCO. The corner-sharing CrO_6 octahedra and spatially isolated MnO_4 squares are shown. Atomic positions: Bi $2a(0, 0, 0)$, Mn $6b(0.5, 0.5, 0)$, Cr $8c(0.25, 0.25, 0.25)$, and O $24g(x, y, 0)$. b) Synchrotron X-ray diffraction pattern and the refinement results. The observed (red circles), calculated (blue line), and difference (cyan line) were shown. The ticks indicate the allowed Bragg reflections in $Im\bar{3}$ symmetry.

at 300 K as well as the refinement results. The Rietveld analysis illustrates that BMCO crystallizes in an $\text{AA}'_3\text{B}_4\text{O}_{12}$ -type A-site ordered quadruple perovskite structure with a centrosymmetric space group $Im\bar{3}$. According to the refined Mn–O and Cr–O bond lengths (see Table S1, Supporting Information), the bond-valence sum calculations indicate that the valence states of Mn and Cr are both close to +3, suggesting the $\text{Mn}^{3+}/\text{Cr}^{3+}$ charge combination in BMCO. Furthermore, the charge states of $\text{Mn}^{3+}/\text{Cr}^{3+}$ can be confirmed by X-ray absorption spectroscopy (XAS) as shown in Figure S2 (Supporting Information). On the basis of the Rietveld analysis of NPD pattern, the occupancy factors for all atoms are very close to unity. The SXR, XAS, and NPD results therefore all reveal the stoichiometric chemical composition for our high-pressure product BMCO. Moreover, temperature dependent SXR (100–300 K), NPD (3–150 K), and SAED (100 and 300 K)

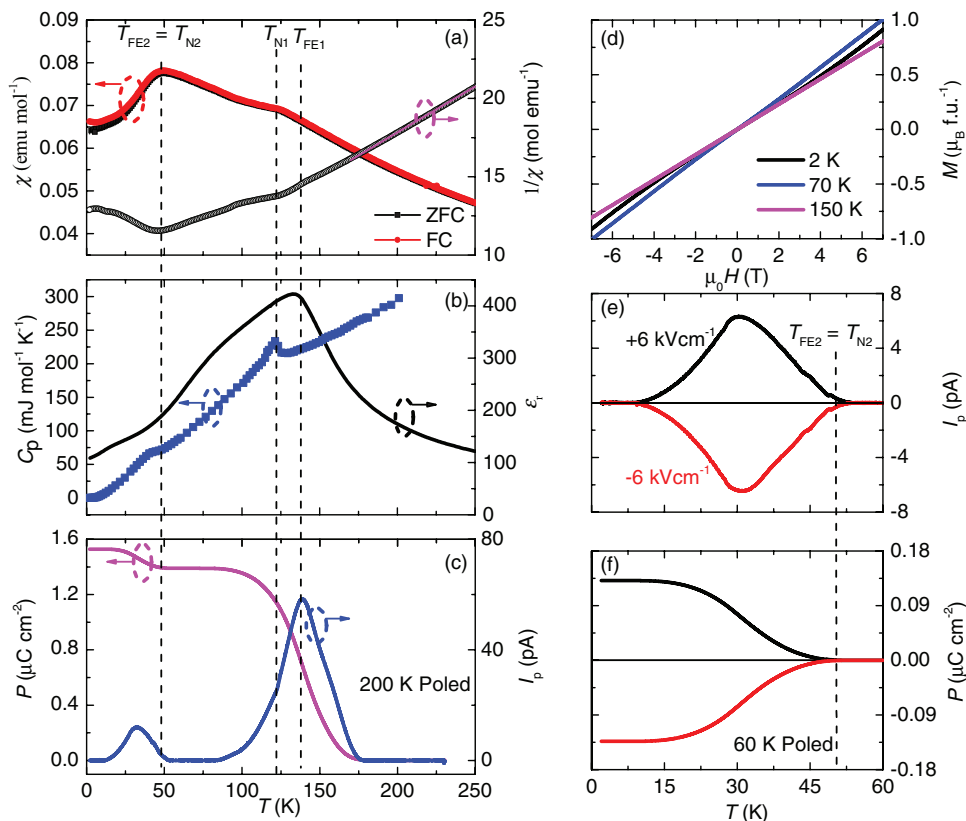


Figure 2. a) Temperature dependent magnetic susceptibility χ and its inverse χ^{-1} with 0.1 T measurement magnetic field. The solid line in the χ^{-1} plot shows the Curie–Weiss law fitting above 170 K. b) Temperature dependence of relative dielectric constant ϵ_r and specific heat C_p at zero magnetic field. c) Temperature dependence of I_p and P poled from 200 K down to 2 K under $+6 \text{ kV cm}^{-1}$. d) The isothermal magnetization behaviors at selected temperatures. Temperature dependence of e) I_p and f) P below 60 K by poling from 60 K down to 2 K. The P was calculated by integrating the I_p as a function of time. The sign of I_p and P can be reversed symmetrically by changing the sign of poling field.

do not show distinguishable trace for macroscopic crystal structural variation with temperature down to 3 K in BMCO (see Figures S3–S5, Supporting Information).

Figure 2a shows the temperature dependence of magnetic susceptibility (χ) of our polycrystalline BMCO. Two AFM transitions are observed with decreasing temperature at $T_{N1} \approx 125$ K and $T_{N2} \approx 48$ K, respectively. The linear and nonhysteresis magnetization behaviors observed below T_{N1} and/or T_{N2} are typical for the AFM ordering (Figure 2b). Above 170 K, the data of χ^{-1} can be well fitted by using the Curie–Weiss law $\chi^{-1} = (T - \theta)/C$. The obtained negative Weiss temperature ($\theta = -104.1$ K) is indicative of the AFM interactions. According to the fitted Curie constant ($C = 17.06 \text{ emu K mol}^{-1}$), the effective moment μ_{eff} is calculated to be $11.68 \mu_B \text{ f.u.}^{-1}$, agreeing well with the theoretical spin-only value ($11.48 \mu_B \text{ f.u.}^{-1}$) for the high-spin Mn^{3+} and Cr^{3+} ions. Corresponding to the two AFM transitions, strong λ -shape anomalies are also observed in specific heat around T_{N1} and T_{N2} (Figure 2c), indicating the second-order nature of these two transitions. As shown later, the NPD analysis reveals that the long-range AFM ordering of the B-site Cr^{3+} sublattice is responsible for the magnetic transition at 125 K, while the lower-temperature one arises from the AFM ordering of the A'-site Mn^{3+} sublattice.

Although BMCO and LMCO have similar crystal structure^[20] and spin orderings,^[16] BMCO exhibits distinguishing dielectric

and FE properties, as presented in Figure 2b,c. The relative dielectric constant ϵ_r of BMCO is over 110, while that of LMCO is about 5.^[16] It means that the ϵ_r of BMCO increases by about 2 orders of magnitude, making the sharp step-like anomaly observed in LMCO around T_{N2} obscure in the current BMCO (Figure 2b). In contrast, the ϵ_r of BMCO shows a clear peak around 135 K at all the frequencies we used for measurements (Figure 2b; and Figure S6a, Supporting Information). With further increasing temperature, the ϵ_r quickly decreases, especially for frequencies above 10 kHz. Note that above ≈ 220 K, the low-frequency dielectric data show upturn features with enhanced dielectric loss, implying the presence of leakage currents at higher temperatures far above the dielectric peak around 135 K (Figure S6a,b, Supporting Information). Anyway, the overall temperature dependent ϵ_r strongly indicates a high-temperature paraelectric to low-temperature ferroelectric phase transition at $T_{FE1} \approx 135$ K.

To confirm the ferroelectricity below T_{FE1} , the pyroelectric current (I_p) is measured after poling the sample from 200 to 2 K. To our surprise, the I_p shows two apparent transitions as shown in Figure 2c. One occurs at the onset about 170 K and is centered at T_{FE1} . The other sets in near T_{N2} and forms a peak around 31 K. Moreover, the sign of I_p is completely reversible by changing the sign of the poling electric field (see Figure S7a,c, Supporting Information), confirming the double FE phase transitions. Since the high-temperature I_p peak is well

consistent with the dielectric peak mentioned above at $T_{FE1} \approx 135$ K, this value is temporarily assigned as the critical temperature for the higher-temperature long-range FE phase (FE1 phase) transition, although some short-range FE domains may emerge below the onset temperature of 170 K for this phase (see P - E loops shown later). In addition, taking into account that the lower-temperature I_p anomaly just sets in at T_{N2} , where the peculiar spin ordering can induce another FE phase (FE2 phase) transition (discussed later). The T_{N2} ($=T_{FE2}$) is thus defined as the critical temperature for FE2 phase. By integrating the I_p with respect to the time, the temperature dependence of electric polarization is obtained as shown in Figure 2c. The value of P is as large as $1.39 \mu\text{C cm}^{-2}$ via the FE1 phase transition and then is further enhanced by $0.14 \mu\text{C cm}^{-2}$ through the FE2 phase transition.

As mentioned above, the FE2 phase takes place near T_{N2} , suggesting an intimate correlation with the AFM ordering. Neutron powder diffraction was thus carried out to link the special spin structure and the FE2 phase. The magnetic Rietveld analysis (Figure S8, Supporting Information) shows that below T_{N1} the B-site Cr^{3+} ions are ordered antiferromagnetically with a collinear G-type spin alignment. Between T_{N1} and T_{N2} , there is no long-range spin order for the A'-site Mn^{3+} ions, but they also become ordered with the similar G-type AFM manner when temperature decreases to T_{N2} . The detailed spin structure of BMCO is illustrated in Figure S1 (Supporting Information). The refined nuclear and magnetic structure parameters of BMCO from the NPD are listed in Table S2 (Supporting Information). Based on the magnetic point group analysis similar with that of LMCO,^[16] the total spin structure composed of the G-type AFM Cr^{3+} and Mn^{3+} sublattices in BMCO possesses a polar magnetic point group 3, which can break the space inversion symmetry and cause a spin-induced ferroelectricity at T_{N2} ($=T_{FE2}$) via the anisotropic symmetric exchange mechanism as described in detail elsewhere.^[17] Therefore, an independent FE phase is expected from the special AFM spin structure of BMCO, indicating the occurrence of type-II MF phase below T_{N2} .

To further reveal the independent AFM-induced FE2 phase occurring at T_{N2} , the poling electric field is applied from 60 to 2 K to across T_{N2} alone. The pyroelectric current is measured and temperature dependent polarization is calculated below 60 K, as shown in Figure 2e,f. One can also find electric field reversible polarization in this case and the magnitude of P ($=0.13 \mu\text{C cm}^{-2}$) is similar with the change of the P below T_{N2} in 200 K poled case in Figure 2c. These results confirm that below T_{N2} , there is an independent spin-induced FE phase (i.e., the FE2 phase), which coexists with the intrinsic high-temperature FE1 phase as stated below.

Since the pyroelectric current measurements may contain some extrinsic contributions such as thermal stimulated current,^[21] ferroelectric hysteresis loops are measured to further confirm the existence of FE1 phase by using the so-called positive-up negative-down (PUND) method (for details, see the Experimental and Theoretical Section). This method can give rise to the intrinsic polarization and remove other extrinsic contributions in normal P - E or pyroelectric current measurement.^[22,23] As shown in Figure 3a, canonical hysteresis loops as presented in conventional FE materials are observed in our

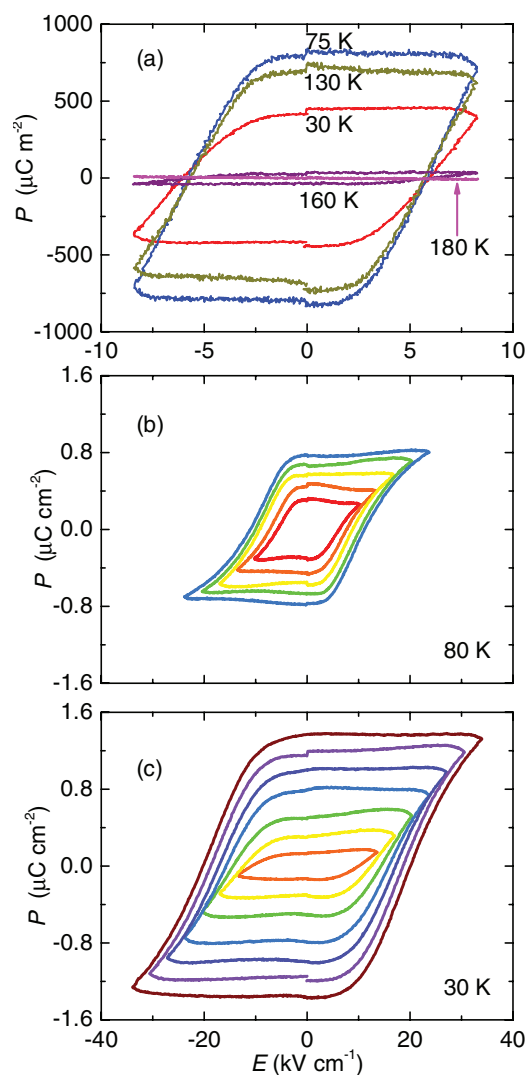


Figure 3. a) The P - E hysteresis loops measured at selected temperatures by using the PUND method. The P - E loops measured at b) 80 K and c) 30 K under selected electric fields.

polycrystalline BMCO at temperatures below T_{FE1} . Between T_{FE1} and the onset temperature 170 K, a small amount of FE hysteresis behavior also shows up, probably implying the presence of some short-range FE domains. The reduction of remanent polarization P_r between 75 and 30 K is also observed (see Figure 3a). This can be attributed to the enhanced coercive field at lower temperature. Figure 3b,c shows the P - E loops measured at 80 K (i.e., in the FE1 phase) and 30 K (in the FE1 + FE2 region), respectively. When the same maximum scanning electric field is applied, the shape of P - E loop measured at 80 K is obviously thinner than that at 30 K, indicating that the coercive field becomes larger when the FE2 phase develops below T_{N2} . At fixed temperatures, the P - E loops significantly expand with increasing maximum electric field. For example, at 30 K, P_r obtained from the PUND loops increases from 0.35 to $1.4 \mu\text{C cm}^{-2}$ as the maximum electric field changes from 17 to 34 kV cm^{-1} (Figure 3c). These results convincingly confirm the intrinsic nature for the high-temperature FE1 phase as well

as the different origins for these two FE phases. Note that at present we could not apply enough high electric field to fully saturate the P due to the slight leakage effect in the polycrystalline BMCO.

Since the FE1 phase occurs well above T_{N1} and T_{N2} , one can exclude magnetic origin for this phase. Our low-temperature SXRD (Figure S3, Supporting Information), NPD (Figure S4, Supporting Information), and SAED (Figure S5, Supporting Information) do not show any evidence for the long-range crystal structural variation in the limits of these experimental resolutions, so the FE1 phase on the one hand probably arises from some microscopic or local structure changes related to the lone-pair effects of Bi^{3+} ions. Actually, when we examine the thermal parameter of Bi^{3+} derived from the high-resolution SXRD refinements using the cubic $Im\bar{3}$ space group (Figure S9, Supporting Information), it just slightly changes above T_{FE1} , whereas drastically drops below this critical temperature. This is reminiscent of the FE polarization caused by the lone-pair electrons like Bi^{3+} and Pb^{2+} due to the off-center distortions, as observed in the perovskites $\text{Pb}_2\text{MgTeO}_6$,^[24] Pb_2CoWO_6 ,^[25] and Pb_2MgWO_6 ,^[26] where the related thermal parameters are also clearly reduced via a paraelectric-to-ferroelectric phase transition.

On the other hand, in order to get deeper insight into the FE1 phase of BMCO, first-principles calculations have been performed. After the optimization of the cubic structure to a high precision, the force constants are calculated at the Γ point of Brillouin zone by employing density functional perturbation theory.^[27] There are three imaginary frequencies, whose magnitudes are degenerated at $\approx 24.76 \text{ cm}^{-1}$ (a moderate value). Such imaginary frequencies imply lattice instability, which may lead to ferroelectricity. In particular, the force vectors of these instable modes suggest that the dominating displacements are from Bi ions, along the cubic $a/b/c$ axes. To further confirm these polar distortions, the energy barrier is calculated by moving all ions following one of the imaginary modes. Figure S10 (Supporting Information) shows the calculated energy as a function of Bi's displacement. The energy well is obvious, suggesting that the polar distortion can occur spontaneously at the ground state with a reduced space group of $Imm2$ (No. 44). Here the optimal displacement of Bi corresponding to the lowest energy is about 0.007 \AA , which is a very small value within the resolution limits of synchrotron X-ray, neutron, and electron diffraction methods. Therefore, no long-range structure phase transition is detectable in our experiments. The calculated polarization is about $0.17 \mu\text{C cm}^{-2}$ using the Berry phase method.^[28] Since here the ions' displacements only consider one imaginary frequency as an example, the total polarization may be even larger by considering the collaborative distortions of all possible modes.

Next, we would like to study the ME effects of the polycrystalline BMCO in different FE phases. First, to characterize the ME effect of the spin-induced FE2 phase below $T_{\text{FE2}}/T_{\text{N2}}$, we measured the polarization as a function of temperature under different magnetic fields where the poling electric field is applied from 60 to 2 K to across T_{N2} alone. The temperature dependent polarization caused by the FE2 phase is calculated to be $P_{\text{FE2}} = P(T) - P(50 \text{ K})$. As shown in Figure 4a, at zero magnetic field, the P_{FE2} value is found to be about $0.19 \mu\text{C cm}^{-2}$, which is

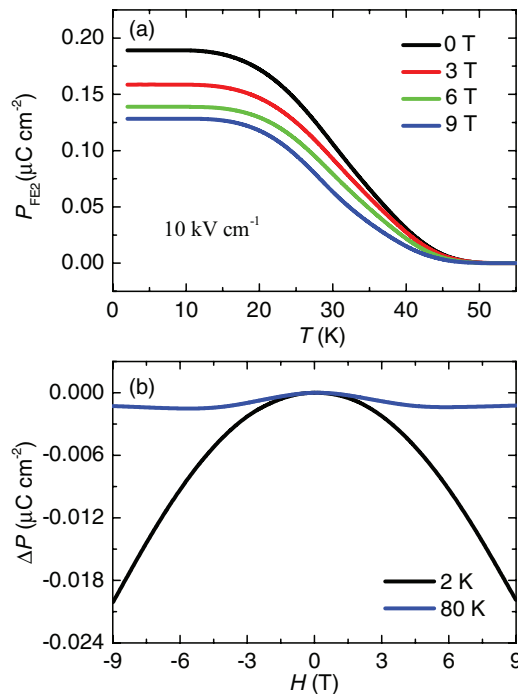


Figure 4. a) The electric polarization $P_{\text{FE2}} = P(T) - P(50 \text{ K})$ obtained at selected magnetic fields perpendicular to the poling electric field. b) The change of polarization ΔP of BMCO as a function of magnetic field at selected temperatures.

significantly larger than that observed in the isostructural LMCO polycrystalline sample ($1.5 \times 10^{-3} \mu\text{C cm}^{-2}$) as well as most type-II MF such as the well-studied TbMnO_3 ($0.08 \mu\text{C cm}^{-2}$)^[13] and TbMn_2O_5 ($0.04 \mu\text{C cm}^{-2}$)^[29] single crystals. When the magnetic field is applied perpendicular to the poling electric field, the polarization is reduced remarkably. We then calculate the ME coefficient for the FE2 phase with an α value up to 85 ps m^{-1} at 9 T and 2 K. Since the temperature-dependent pyroelectric measurements may involve some extrinsic contributions such as thermal stimulated current, we also at fixed temperatures performed magnetic field dependent ME current measurements. To rule out the extrinsic contribution, we use the relative $\Delta P [=P(H) - P(0 \text{ T})]$ instead of P to compare the ME effects in different FE phases. Figure 4b shows the H dependence of ΔP at selected temperatures. Above T_{N2} (e.g., at 80 K), the ΔP is quite small and almost H independent. In sharp contrast, below T_{N2} (e.g., at 2 K), the value of ΔP sharply decreases with increasing H and is roughly in proportion to H^2 up to 9 T. The maximum α value is calculated to be 71 ps m^{-1} at 9 T and 2 K, slightly smaller than that estimated from the temperature-dependent pyroelectric measurements under constant H . The distinct ME behaviors between the two FE phases (see Figure 4b) strongly indicate the different microscopic origins of their polarization. By comparison, the ME effect in FE2 phase measured on the present polycrystalline BMCO is considerably stronger than that observed in the type-I MF materials like BiFeO_3 single crystal ($<5 \text{ ps m}^{-1}$) as well as the type-II MF materials such as polycrystalline TbMnO_3 ($\approx 13 \text{ ps m}^{-1}$ at 4 T)^[30] and single-crystal TbMn_2O_5 ($\approx 21 \text{ ps m}^{-1}$ at 2 T).^[31] Therefore, BMCO not only possesses a large polarization but also a strong ME effect.

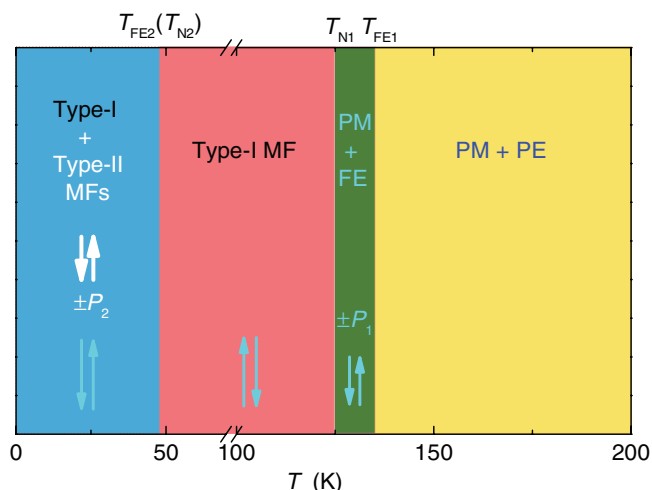


Figure 5. Magnetic and electric evolution as a function of temperature in $\text{BiMn}_3\text{Cr}_4\text{O}_{12}$. PM, PE, FE, and MF denote paramagnetic, paraelectric, ferroelectric, and multiferroic phases, respectively. P_1 and P_2 stand for the ferroelectric polarization generated by the FE1 and FE2 phases, respectively.

We now figure a fascinating magnetic and electric evolution with temperature for the cubic perovskite BMCO. As shown in **Figure 5**, at temperatures above $T_{\text{FE1}} \approx 135$ K, BMCO shows paramagnetic and paraelectric behaviors (some short-range FE domains may develop between T_{FE1} and 170 K). On cooling to T_{FE1} , a FE phase transition (FE1 phase) takes place, and the material is featured by long-range ferroelectricity and paramagnetism between T_{FE1} and $T_{\text{N1}} \approx 125$ K. Then, the B-site Cr^{3+} spins become ordered at T_{N1} . It means that both long-range spin ordering and FE polarization coexist at temperatures $T_{\text{N1}} > T > T_{\text{N2}} \approx 48$ K, so the compound develops into a type-I multiferroic phase in this temperature window with a huge polarization about $1.4 \mu\text{C cm}^{-2}$ as evaluated from the PUND P - E loops (Figure 3d). According to theoretical calculation, this P vector will point to [001] or its equivalent directions. Once the AFM spin ordering of the A'-site Mn^{3+} is formed near T_{N2} , a spin-induced FE phase (FE2 phase) occurs, leading to the presence of a type-II multiferroic phase with considerable ME coupling. The P vector of FE2 phase points to [111] direction on the basis of magnetic point group analysis.^[16] Since double multiferroic phases occur in BMCO, one can obtain four different polarization states ($\pm P_1, \pm P_2$)^[31,32] below T_{FE2} by applying different poling E procedures (see Figure 5; and Figure S7, Supporting Information). For example, applying $+E$ from 200 to 55 K and $-E$ from 55 to 2 K poling procedures result in a $(+P_1, -P_2)$ state. Such quadruple polarization states are essentially different from the reported ME states ($\pm P, \pm M$) observed in other MF materials,^[33–37] opening up a novel arena to realize multistate memories. The current BMCO presents a rare example of single-phase multiferroic system where both type-I and type-II multiferroic phases coexist in a cubic perovskite structure. In sharp contrast to previous findings, the large electric polarization and strong ME effect are compatible in BMCO, providing a new pathway for generating advanced MF materials and devices.

Supporting Information

Supporting Information is available from the Wiley Online Library or from the author.

Acknowledgements

The authors thank X.Q. Chen, H.J. Xiang, J.J. Zhang, and Z.G. Sheng for fruitful discussion. This work was partly supported by 973 Project of the Ministry of Science and Technology of China (Grant No. 2014CB921500), the NSFC (Grant Nos. 11574378, 51772324, 11534015, and 51322206), and the Chinese Academy of Sciences (Grant Nos. QYZDB-SSW-SLH013, XDB07030300, YZ201555, and GJHZ1773), Research conducted at ORNL's High Flux Isotope Reactor was sponsored by the Scientific User Facilities Division, Office of Basic Energy Sciences, US Department of Energy. Y. W. Long thanks the support of World Research Hub Initiative, Institute of Innovative Research, Tokyo Institute of Technology, Collaborative Research Projects, Laboratory for Materials and Structures, Tokyo Institute of Technology and Kanagawa Institute of Industrial Science and Technology.

Conflict of Interest

The authors declare no conflict of interest.

Keywords

A-site ordered perovskite, high-pressure synthesis, magnetoelectric coupling, multiferroic

Received: June 19, 2017
Revised: August 25, 2017
Published online: October 9, 2017

- [1] H. Schmid, *Ferroelectrics* **1994**, *162*, 317.
- [2] N. A. Spaldin, M. Fiebig, *Science* **2005**, *309*, 391.
- [3] W. Eerenstein, N. D. Mathur, J. F. Scott, *Nature* **2006**, *442*, 759.
- [4] S. W. Cheong, M. Mostovoy, *Nat. Mater.* **2007**, *6*, 13.
- [5] R. Ramesh, N. A. Spaldin, *Nat. Mater.* **2007**, *6*, 21.
- [6] J. Ma, J. M. Hu, Z. Li, C. W. Nan, *Adv. Mater.* **2011**, *23*, 1062.
- [7] Y. Tokura, S. Seki, N. Nagaosa, *Rep. Prog. Phys.* **2014**, *77*, 076501.
- [8] S. Dong, J. M. Liu, S. W. Cheong, Z. F. Ren, *Adv. Phys.* **2015**, *64*, 519.
- [9] D. Khomskii, *Physics* **2009**, *2*, 20.
- [10] J. Wang, J. B. Neaton, H. Zheng, V. Nagarajan, S. B. Ogale, B. Liu, D. Viehland, V. Vaithyanathan, D. G. Schlom, U. V. Waghmare, N. A. Spaldin, K. M. Rabe, M. Wuttig, R. Ramesh, *Science* **2003**, *299*, 1719.
- [11] Y. F. Popov, A. M. Kadomtseva, S. S. Krotov, D. V. Belov, G. P. Vorob'ev, P. N. Makhov, A. K. Zvezdin, *Low Temp. Phys.* **2001**, *27*, 478.
- [12] I. A. Sergienko, C. Sen, E. Dagotto, *Phys. Rev. Lett.* **2006**, *97*, 227204.
- [13] T. Kimura, T. Goto, H. Shintani, K. Ishizaka, T. Arima, Y. Tokura, *Nature* **2003**, *426*, 55.
- [14] Y. Tokura, Y. Seki, *Adv. Mater.* **2010**, *22*, 1554.
- [15] Y. Tokura, Y. Seki, Z. Nagaosa, *Rep. Prog. Phys.* **2014**, *77*, 076501.
- [16] X. Wang, Y. S. Chai, L. Zhou, H. B. Cao, C. Cruz, J. Y. Yang, J. H. Dai, Y. Y. Yin, Z. Yuan, S. J. Zhang, R. Z. Yu, M. Azuma, Y. Shimakawa, H. M. Zhang, S. Dong, Y. Sun, C. Q. Jin, Y. W. Long, *Phys. Rev. Lett.* **2015**, *115*, 087601.
- [17] J. S. Feng, H. J. Xiang, *Phys. Rev. B* **2016**, *93*, 174416.

- [18] J. R. Teague, R. Gerson, W. J. James, *Solid State Commun.* **1970**, *8*, 1073.
- [19] Y. N. Zakharov, I. P. Raevski, E. I. Eknadiosians, A. N. Pinskaya, L. E. Pustovaya, V. Z. Borodin, *Ferroelectrics* **2000**, *247*, 47.
- [20] Y. W. Long, T. Saito, M. Mizumaki, A. Agui, Y. Shimakawa, *J. Am. Chem. Soc.* **2009**, *131*, 16244.
- [21] K. Cho, S. Hur, S. Park, *Appl. Phys. Lett.* **2017**, *110*, 162905.
- [22] J. F. Scott, L. Kammerdiner, M. Parris, S. Traynor, V. Ottenbacher, A. Shawabkeh, W. F. Oliver, *J. Appl. Phys.* **1988**, *64*, 787.
- [23] Y. S. Chai, Y. S. Oh, L. J. Wang, N. Manivannan, S. M. Feng, Y. S. Yang, L. Q. Yan, C. Q. Jin, K. H. Kim, *Phys. Rev. B* **2012**, *85*, 184406.
- [24] G. Baldinozzi, D. Grebille, Ph. Sciau, J. M. Kiat, J. Moret, J. F. Bézar, *J. Phys.: Condens. Matter* **1998**, *10*, 6461.
- [25] M. Bonin, W. Paciorek, K. J. Schenk, G. Chapuis, *Acta Cryst. B* **1995**, *51*, 48.
- [26] J. Blasco, R. I. Merino, J. Garcia, M. C. Sanchez, *J. Phys.: Condens. Matter* **2006**, *18*, 2261.
- [27] S. Baroni, S. de Gironcoli, A. Dal Corso, *Rev. Mod. Phys.* **2001**, *73*, 515.
- [28] R. Resta, *Rev. Mod. Phys.* **1994**, *66*, 899.
- [29] L. C. Chapon, G. R. Blake, M. J. Gutmann, S. Park, N. Hur, P. G. Radaelli, S.-W. Cheong, *Phys. Rev. Lett.* **2004**, *93*, 177402.
- [30] Y. Y. Guo, Y. L. Wang, J. M. Liu, T. Wei, *J. Appl. Phys.* **2014**, *116*, 063905.
- [31] N. Hur, S. Park, P. A. Sharma, J. S. Ahn, S. Guha, S.-W. Cheong, *Nature* **2003**, *429*, 392.
- [32] B. Van Aken, T. T. M. Palstra, A. Filippetti, N. A. Spaldin, *Nat. Mater.* **2004**, *3*, 164.
- [33] N. Leo, D. Meier, R. V. Pisarev, N. Lee, S. W. Cheong, M. Fiebig, *Phys. Rev. B* **2012**, *85*, 094408.
- [34] R. D. Johnson, L. C. Chapon, D. D. Khalyavin, P. Manuel, P. G. Radaelli, C. Martin, *Phys. Rev. Lett.* **2012**, *108*, 067201.
- [35] G. Q. Zhang, S. Dong, Z. B. Yan, Y. Y. Guo, Q. F. Zhang, S. J. Yunoki, E. Dagotto, J. M. Liu, *Phys. Rev. B* **2011**, *84*, 174413.
- [36] N. Ikeda, H. Ohsumi, K. Ohwada, K. Ishii, T. Inami, K. Kakurai, Y. Murakami, K. Yoshii, S. Mori, Y. Horibe, H. Kitô, *Nature* **2006**, *436*, 1136.
- [37] L. C. Chapon, P. G. Radaelli, G. R. Blake, S. Park, S. W. Cheong, *Phys. Rev. Lett.* **2006**, *96*, 097601.